

## Article

# A New Method of Fault Localization for 500 kV Transmission Lines Based on FRFT-SVD and Curve Fitting

Mohamed H. Saad <sup>1,\*</sup> , Mostafa M. Fouda <sup>2,3,\*</sup>  and Abdelrahman Said <sup>3</sup> 

<sup>1</sup> Radiation Engineering Department, National Center for Radiation Research and Technology (NCRRT), Egyptian Atomic Energy Authority, Cairo 11672, Egypt

<sup>2</sup> Department of Electrical and Computer Engineering, College of Science and Engineering, Idaho State University, Pocatello, ID 83209, USA

<sup>3</sup> Department of Electrical Engineering, Faculty of Engineering at Shoubra, Benha University, Cairo 11672, Egypt

\* Correspondence: m.hassansaad@eaea.sci.eg (M.H.S.); mfouda@ieee.org (M.M.F.)

**Abstract:** The paper presents the Fractional Fourier Transform-Singular Value Decomposition (FRFT-SVD) method for the localization of various power system faults in a 200 km long, 500 kV Egyptian transmission line using sent end-line current signals. Transient simulations are carried out using Alternating Transient Program/Electromagnetic Transient Program (ATP-EMTP), and the outcomes are then examined in MATLAB to carry out a sensitivity analysis against measurement noises, sampling frequency, and fault characteristics. The proposed work employs current fault signals of five distinct kinds at nineteen intermediate points throughout the length of the line. The approach utilized to construct the localizer model is FRFT-SVD. It is much more effortless, precise, and effective. The FRFT-SVD is utilized in this technique to calculate 19 sets of indices of the greatest S value throughout the length of the line. The FRFT-SVD localizer model is also designed to be realistic, with power system noise corrupting fault signals. To generate fault curves, the curve fitting technique is applied to these 19 sets of indices. Reduced chi-squared and modified R-squared criteria are used to choose the best-suited curve. The proposed work results in a very precise localization, with only a 0.0016% average percentage error for fault localization and a maximum percentage error of 0.002% for the 200 km Egyptian transmission line. Finally, this work can be employed as a proper link between the nuclear power plant and the grid. The proposed method is an efficient fault distance estimation method that might contribute to creating a dependable transient-based approach to power system protection.

**Keywords:** fault location; ATP-EMTP; long transmission line; curve fitting techniques; FRFT-SVD



**Citation:** Saad, M.H.; Fouda, M.M.; Said, A. A New Method of Fault Localization for 500 kV Transmission Lines Based on FRFT-SVD and Curve Fitting. *Energies* **2023**, *16*, 758. <https://doi.org/10.3390/en16020758>

Academic Editor: Pawel Rozga

Received: 10 December 2022

Revised: 4 January 2023

Accepted: 6 January 2023

Published: 9 January 2023



**Copyright:** © 2023 by the authors. Licensee MDPI, Basel, Switzerland. This article is an open access article distributed under the terms and conditions of the Creative Commons Attribution (CC BY) license (<https://creativecommons.org/licenses/by/4.0/>).

## 1. Introduction

In deregulated situations, accurate fault location in transmission lines saves power system recovery time, associated costs, and financial losses. Three techniques are used to locate faults in the electrical grid: approaches based on impedance [1,2], traveling wave fault location [3–5], and artificial intelligence [6–10]. While traveling wave-based methods employ high-frequency transient components produced by fault or switching operations, impedance-based methods utilize power frequency components of voltages and currents. Artificial intelligence (AI) and machine learning (ML) techniques are typically the foundation of soft computing. Singular value decomposition (SVD) techniques have drawn greater attention in recent years thanks to developments in signal processing, the ability to sample signals at high frequencies, and the creation of optical sensors. Voltage, current, power, frequency, etc., are only a few of the many variable factors of the power system as a whole. The application of SVD can reduce the size of these electrical characteristics, making it easier, faster, and more accurate to determine fault features. Furthermore, SVD is extremely efficient when dealing with noisy data. Consequently, it reduces the

unpredictability of noise, making SVD more suitable for application in a noisy setting such as the power system.

The FRFT-SVD approach, which is exceedingly effective, accurate, and simple to use, was employed to construct the localizer model. To determine the characteristics of a signal in terms of the maximum S value, which is employed in this approach to calculate the indices, FRFT-SVD is a straightforward technique. In particular, for more decomposition, wavelet transform-based analysis becomes more challenging. On the other hand, neural networks need a lot of training data that are spread out over a long period of time. As a result, the proposed fault localizer is both very precise and fast. The proposed analysis might be enhanced to include fault localization in a transmission network or a system with several interconnected buses. In the event of such a system, it is first necessary to determine the bus from which the line with the problem originated. After conducting the following fault localization study, that bus might be taken as the source point. This study's goal is to provide a technique for the efficient use of curve fitting analysis and FRFT-SVD for the sole purpose of fault site prediction.

### 1.1. Related Work

Scientists have used quick fault detection, classification, and location identification techniques to guarantee system stability and safety [11].

To restore the system stability in a power transmission network, the faulty phase or phases must be removed. Numerous computational tools for defect diagnostics have been created by researchers. As previously noted, the proposed work investigates the function of SVM as an upgrading simulation tool and uses it to create a fault location technique.

For the detection, categorization, and localization of faults, researchers have created numerous mathematical and computational algorithms. Nowadays, researchers use artificial intelligence (AI) widely in the study of power systems and fault analysis. One of the most popular and important techniques for studying the protection of transmission lines in power systems has been the Artificial Neural Network (ANN) and its various variations [12].

One of the most recent developments in this area is the use of neural networks for analysis powered by extreme learning machines (ELMs) [13]. As a conventional approach to fault signal analysis, Wavelet Transform (WT) has been crucial in numerous studies of fault analysis, even using contemporary compensating devices [14].

Another useful tool for fault analysis is the fuzzy inference system, which is frequently employed as a primary analytical technique alone [15], as well as in a hybrid model with wavelet analysis [16] and neural networks, known as the (ANFIS) model. To create wavelet-based ANFIS models and as a useful means of comprehensive analysis, this hybrid model has frequently been supported by WT analysis [17]. As a significant standalone method of study, (SVM) has also been utilized in numerous studies pertaining to power system protection algorithms [18].

A simple approach to classifying and locating power system defects was developed using principal component analysis (PCA). For the quick location of the faulty line, this work solely employs 14-cycle pre-fault and 12-cycle post-fault receiving side current waveforms.

Although SVM-based algorithms are also highly popular for fault analysis, they nevertheless have the issue of intensive training because of noise contamination to some extent.

Both [19] and [20] authors explore faults in OHTL with various sources linked to the system, whereas [19] authors present a method for fault identification intended for busbar zone protection, as demonstrated by the authors of [21], who provided polynomial and Gaussian radial basis functions (RBF) for fault classification, or [22], who used dyadic WT-based SVM for fault classification.

The authors of [23] use time-synchronized fault signals as modern research tools.

Other new research inclusions include measurement analysis based on magnetic flux variation [24], feature extraction techniques based on mathematical morphology [25],

ensemble Kalman filter-based strategies [26], analysis based on the combination of several sensors and fuzzy inference [27], monitoring of transmission line [28–30], etc.

Several more methodologies can help with the development of fault analysis strategies. Considering this, the purpose of this study is to provide a technique for the efficient use of curve fitting analysis and FRFT-SVD only for fault site prediction. Consequently, the analysis is conducted with a variable fault resistance, various fault inception angles, and noise. The paper proposes the Fractional Fourier Transform-Singular Value Decomposition (FRFT-SVD) approach for localizing various power system problems in a 200 km long, 500 kV Egyptian transmission line under varied operating conditions utilizing received end-line current data. The proposed method has all the potential to become an efficient way of predicting the distance to a fault, which may help in the creation of a dependable transient-based power system protection strategy.

### *1.2. Motivation and Contributions*

The numerous AT-detection technologies that have recently been introduced each have drawbacks. For instance, the choice of the mother wavelet affects DWT performance. Due to the aliasing phenomena, the Empirical Mode Decomposition (EMD) process has the potential to affect HHT performance. Wavelet transform-based analysis becomes increasingly complicated as the depth of decomposition increases. On the other hand, neural networks need extensive training time and widely dispersed training data.

In this paper, a new method for fault location based on FRFT-SVD and curve fitting of 500 kV long transmission lines is proposed. The purpose of this work is to provide a strategy for the efficient use of curve fitting analysis and FRFT-SVD for fault site prediction only. This method lacks the shortcomings of the methods listed above because it was designed based on algebraic operations in the time-frequency domain. The suggested algorithm addresses the finding of defects for all fault kinds under various operational scenarios. Simulations are run in the EMTP/ATP program, and the results are analyzed in MATLAB to assess how well the proposed technique performs. Through comprehensive simulations, the sensitivity analysis of measurement noises, sample frequency, and fault parameters is examined. The results of FRFT-SVD and curve fitting are examined, and the suggested method's proper operation under various circumstances is demonstrated. Following is a summary of the suggested method's key characteristics: (1) It is sufficiently resilient against noise. (2) It is simple to implement and has a straightforward structure. (3) Because it uses straightforward algebraic calculations, it runs quickly enough for online applications. (4) It responds appropriately without the need for structural adjustments or training in various systems and circumstances.

### *1.3. Organization*

The organization of the paper is as follows. Section 2 describes the details of the system under study. The study of 500 kV-long transmission line fault signals is presented in Section 3. Section 4 outlines the basic tenets of the suggested detection method. In Section 5, thorough simulations are used to assess how sensitive the suggested strategy is to the system characteristics; a summary of the outcomes of contrasting the suggested method with traditional methods is also provided in Section 5. In Section 6, conclusions are presented.

## **2. System Description and Modelling**

Figure 1 depicts the system under analysis, which is based on a typical 500 kV transmission line in Egypt with a 200 km-long line.

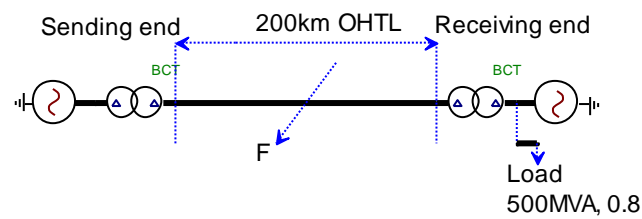


**Figure 1.** A 500 kV transmission line in Egypt with a 200 km-long line.

The most sophisticated JMARTI model, which is a frequency-dependent model and suitable for transients research [31,32], is used to simulate the considered transmission line. Table 1 lists the key characteristics of the transmission system in operation. There are two ground wires with direct tower grounding, and phase conductors are presumed to be perfectly transposed. It is assumed that the soil resistivity is  $100 \Omega\text{m}$  [31]. Figure 2 depicts the conductor arrangements and tower configuration [31].

**Table 1.** The main parameters of the power line.

Items	Value
Line voltage (r.m.s) in kV	500
Line length in km	200
Tower circuit No.	1
Sub-conductors per phase No.	3
Ground wires No.	2
Sub-conductor diameter in mm	30.6
Spacing between sub-conductor in phase in cm	47
Span in meters	400
Diameter of ground wire in mm	11.02

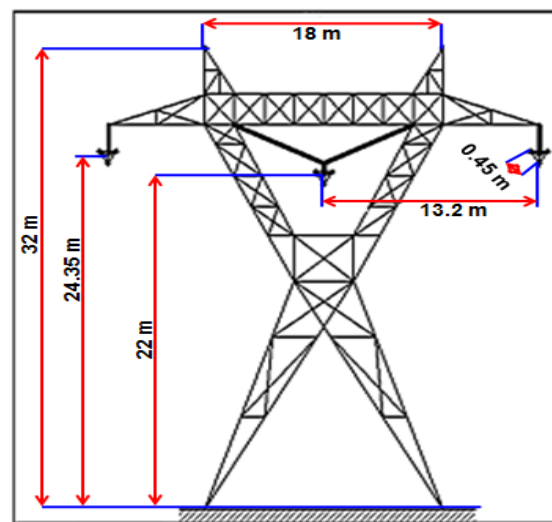


**Figure 2.** Tower configuration and conductor arrangements.

### 3. Analysis of 500 kV OHTL Fault Signals

A practical Egyptian 500 kV OHTL ATP/EMTP simulation uses a 200 km transmission line model. Twenty identical blocks, each 10 km in length, are connected in a cascade to develop the 200 km OHTL model. This designed system is shown in Figure 3. Faults have been conducted at the intermediate junctions of each consecutive block, and the fault current waveforms are recorded at the sending side only. Faults depend on five main fault parameters: (fault type, fault distance, fault resistance, noise, and inception angle).

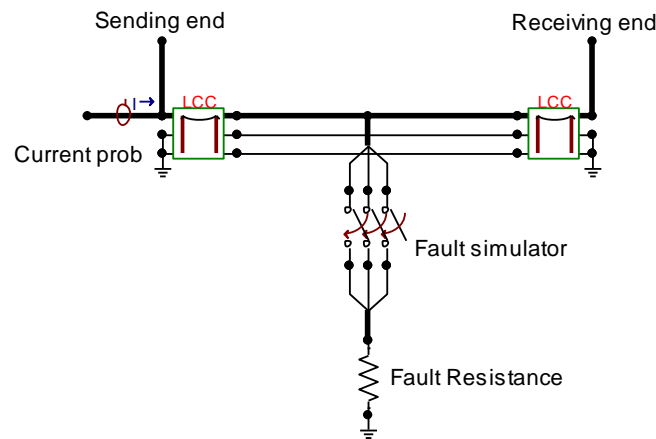


Figure 3. Simulated OHTL model.

Five different fault types (Line to Ground (LG), Line to Line (LL), Line to Line to Ground (LL-G), Line to Line to Line (LLL), and Line to Line to Line to Ground (LLL-G)) are simulated in this regard, together with five fault resistances ( $R$ ), five inception angles ( $\theta$ ) (including  $0^\circ$ – $180^\circ$ ), and 19 distances of the fault from the recording site (including 10 km–190 km). Following the application of LG fault type to the phases at 190 km (before the line’s end) from the transmitting side, Figure 4a–d show the faulted-phase current waveforms at different locations, fault resistance, and inception angles. Figure 4b shows the sending side signals under different locations (with fault resistance =  $10\ \Omega$ , inception angle =  $0^\circ$  and fault location = (10 km, 50 km, 100 km, 150 km, 190 km) for the one-phase (a) to ground fault. It is evident that the faulted phase current signal peak reduced from 25 kA to 5.8 kA, or by about 77%. Figure 4c shows the sending end signals under different  $R$  (with  $R = (1\ \Omega, 10\ \Omega, 25\ \Omega, 35\ \Omega, 50\ \Omega)$ , inception angle =  $0^\circ$  and fault location = 190 Km for the one-phase (a) to ground fault. It is clear that the faulted phase current amplitude reduced from 6.4 kA to 4.1 kA, or by about 36%. Figure 4d show the sending end signals under different inception angle (with fault resistance =  $10\ \Omega$ , Inception Angle  $\theta = (0^\circ$  to  $180^\circ)$ , and fault location = 190 km for the one-phase (a) to ground fault. Moreover, the beginning current amplitude in the case of fault at  $0^\circ$ , and  $45^\circ$  is much more than  $90^\circ$ ,  $135^\circ$ , and  $180^\circ$ .

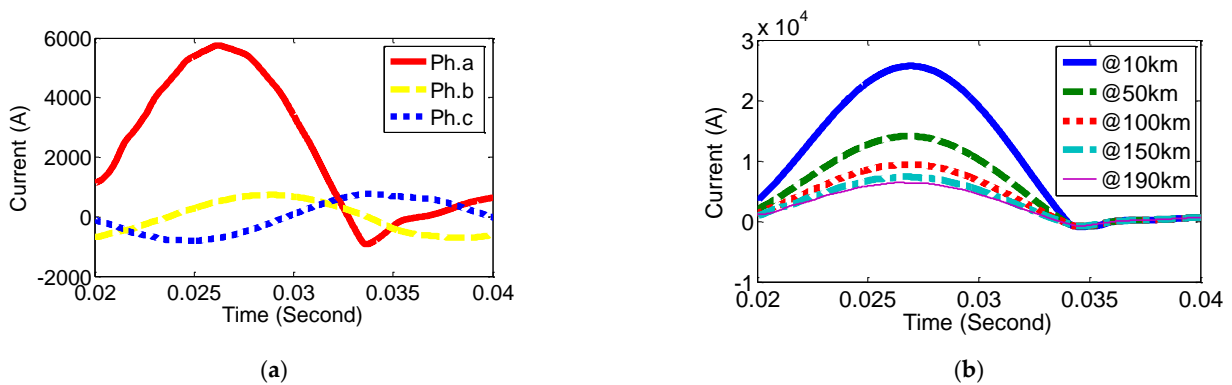


Figure 4. Cont.



where  $\rho$  is the rank of the matrix  $A$ . Note that  $S_1 > S_2 > \dots > S_\rho$ , i.e.,  $S_1$  is the largest singular value. Because SVD has the ability to describe the feature matrix as a collection of values (singular values), it has a dimension-reduction technique. The solitary values also have high stability. In other words, there isn't a significant variation in the singular values of the feature matrix element as it changes.

## 5. Results and Discussion

### 5.1. Data Preparation for the Proposed Algorithm

#### 5.1.1. Data Preparation for Training

The block diagram for the proposed method for power system fault localization using the Fractional Fourier Transform-Singular Value Decomposition (FRFT-SVD) method is shown in Figure 5.

A diagonal matrix produced by SVD over the fault current transients exhibits many of the fundamental properties of the original matrix. The vectors consist of 1500 data points, each with a pre-fault length of quarter cycles and a post-fault length of half cycles, and a sampling frequency of 2000 samples per cycle. As a result, the data matrix is produced as follows:

$$D_{nl} = \begin{bmatrix} ia_{nl1} & ib_{nl1} & ic_{nl1} \\ ia_{nl2} & ib_{nl2} & ic_{nl2} \\ \dots & \dots & \dots \\ ia_{nl1500} & ib_{nl1500} & ic_{nl1500} \end{bmatrix}_{1500 \times 3} \quad (4)$$

Hence,  $D_{nl} = [ia_{nl} \quad ia_{nl} \quad ia_{nl}]_{1500 \times 3}$ .

A fault class is represented by  $n$  denoted by 1, 2, ..., 5, the location of the fault is indicated by  $l$ , and the sample index is indicated by 1, 2, ..., 1500.  $ia_{nl}$ ,  $ib_{nl}$ , and  $ic_{nl}$  indicate the currents for  $n$ -th class. The creation of the proposed fault localization technique makes use of fault data from 19 distinct, evenly spaced fault locations at 10, 20, 30, 40, 50, 60, 70, 80, 90, 100, 110, 120, 130, 140, 150, 160, 170, 180, and 190 km. The input training matrix for the FRFT-SVD becomes

$$\begin{aligned} Da_l &= [ia_{l10} \quad ia_{l20} \dots \quad ia_{l190}]_{1500 \times 19} \\ Db_l &= [ib_{l10} \quad ib_{l20} \dots \quad ib_{l190}]_{1500 \times 19} \\ Dc_l &= [ic_{l10} \quad ic_{l20} \dots \quad ic_{l190}]_{1500 \times 19} \end{aligned} \quad (5)$$

where the training matrix for the  $n$ -class of fault for phases  $a$ ,  $b$ , and  $c$  is represented by  $D_{al}$ ,  $D_{bl}$ , and  $D_{cl}$ . This leads to the formation of five such matrices for each phase. The recommended fault localization methodology uses fault data for 19 distinct, evenly spaced fault sites at 10, 20, 30, 40, 50, 60, 70, 80, 90, 100, 110, 120, 130, 140, 150, 160, 170, 180, and 190 km. With a changeable fault location, the  $S$  matrix contrasts signals from a fixed phase.

#### 5.1.2. Data Preparation for Testing

The preparation of test data is identical as well. The result is the test data matrix, which has an unknown fault location but a known fault class  $t$ :

$$T_{nt} = \begin{bmatrix} ia_{nt1} & ib_{nt1} & ic_{nt1} \\ ia_{nt2} & ib_{nt2} & ic_{nt2} \\ \dots & \dots & \dots \\ ia_{nt1500} & ib_{nt1500} & ic_{nt1500} \end{bmatrix}_{1500 \times 3} \quad (6)$$

Hence,  $T_{nt} = [ia_{nt} \quad ia_{nt} \quad ia_{nt}]_{1500 \times 3}$ , where  $T_{nt}$  is the test data matrix.

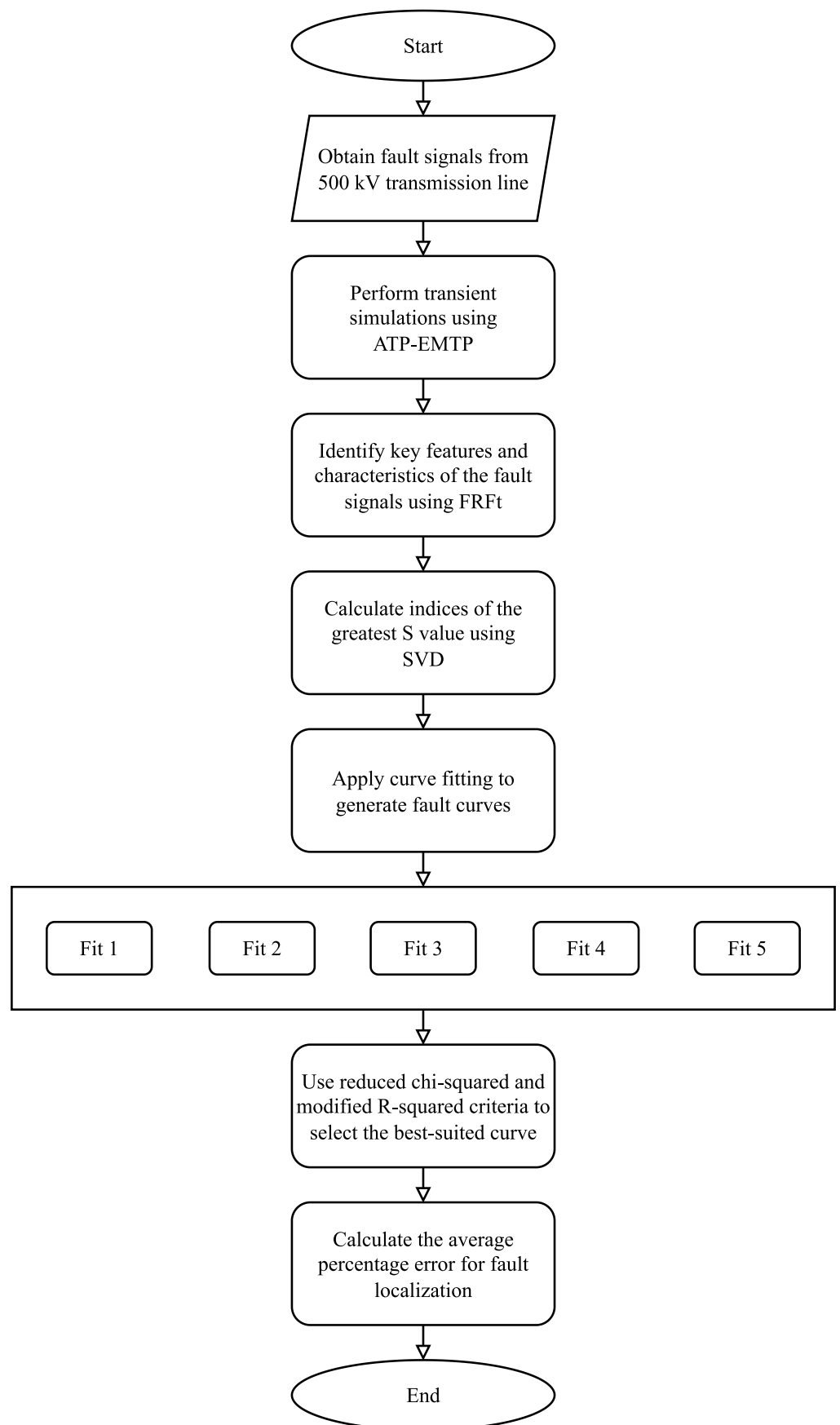


**Figure 5.** The block diagram for the proposed method.

### 5.2. The Impact of Noise, Fault Resistance, and Inception Angle

The fault signals have been combined with Gaussian white noise to create noise-contaminated fault signals. By adjusting the SNR level, the fault waveform noise level can also be adjusted in four steps. The more significant point is that the proposed model is tested at a high noise level of 15 dB SNR, which is higher than the typical noise level used in most research. The impact of this undesirable noise is considered even when variations in fault type, location, and fault resistance occur concurrently. FRFT creates a signal's intermediate time-frequency representations. SVD has a dimension reduction strategy because it expresses the feature matrix as a collection of singular values. Additionally, the singular values are stable. The maximum SVD of the FRFT for a single phase yields a single feature (maximum value S matrix). Three features are chosen for each fault state in OHTL. FRFT-SVD thus eliminates the impact of noise on discrimination. In this work, the noise immunity property is also studied. A comparison of the maximum singular value for direct standardized fault signals and that of its filtered form is shown in Table 2. Additional results are declared in Tables A1–A4. The observations demonstrate that filtering has no discernible impact on the FRFT-SVD algorithm's results, as there is no noticeable change in the magnitude of the max singular value. Using the suggested FRFT-SVD based fault analyzer has this as a major benefit. By doing away with the need for filtering, FRFT-SVD can lessen the computational load. The SNR is varied for this purpose to observe the variation in max singular value, and the proposed algorithm is then run under more challenging conditions with higher noise levels. The maximum singular values in Tables 2 and A1, Tables A2–A4 show how the results of analyzing the filtered and unfiltered signals using maximum singular values are extremely similar. Filtering thus becomes unnecessary at the maximum singular value, saving vital computation and processing time. This demonstrates the inherent ability of FRFT-SVD to largely ignore the effect of noise.

**Table 2.** Max singular value of FRFT-SVD results at various SNRs for direct and filtered signals under LG fault scenario.

Location (km)	SNR = 15 dB		SNR = 20 dB		SNR = 25 dB		SNR = 30 dB	
	Direct	Filtered	Direct	Filtered	Direct	Filtered	Direct	Filtered
10	2,634,600	2,634,602	2,634,601	2,634,601	2,634,603	2,634,601	2,634,602	2,634,601
20	1,317,400	1,317,404	1,317,401	1,317,401	1,317,402	1,317,401	1,317,403	1,317,401
30	878,350	878,356	878,353	878,352	878,351	878,351	878,351	878,352
40	658,810	658,813	658,813	658,813	658,812	658,812	658,812	658,811
50	527,090	527,093	527,091	527,091	527,091	527,092	527,092	527,091
60	439,270	439,275	439,272	439,273	439,273	439,271	439,271	439,272
70	376,540	376,542	376,543	376,541	376,542	376,542	376,544	376,542
80	329,500	329,503	329,501	329,502	329,501	329,501	329,502	329,501
90	292,910	292,914	292,911	292,911	292,911	292,911	292,913	292,912
100	263,630	263,631	263,634	263,631	263,632	263,633	263,631	263,631
110	239,680	239,682	239,683	239,681	239,681	239,682	239,682	239,681
120	219,710	219,711	219,712	219,712	219,712	219,712	219,712	219,712
130	202,820	202,822	202,821	202,821	202,822	202,821	202,821	202,821
140	188,340	188,346	188,341	188,341	188,343	188,343	188,341	188,342
150	175,800	175,801	175,802	175,802	175,801	175,802	175,802	175,801
160	164,820	164,821	164,823	164,824	164,822	164,821	164,823	164,821
170	155,130	155,133	155,132	155,131	155,131	155,132	155,132	155,132
180	146,520	146,521	146,523	146,523	146,521	146,523	146,522	146,521
190	138,810	138,811	138,810	138,812	138,811	138,811	138,810	138,811

The maximum singular values in Tables 3 and A5, Tables A6–A9 show how the results of analyzing the filtered and unfiltered signals using maximum singular values at different fault resistance and inception are extremely similar. The results show that the proposed method is unaffected by changes in fault distance, fault resistance, noise, or fault inception angle. As a result, the proposed algorithm will work in direct form.

**Table 3.** Max singular values of FRFT-SVD results for direct and filtered current signals at various faults and inception angles with  $R = 10 \Omega$ .

Inception Angle		0°		45°		90°		135°		180°	
Faults	Location (km)	Direct	Filtered								
LG	10	2,634,600	2,634,601	2,634,602	2,634,600	2,634,605	2,634,607	2,634,602	2,634,603	2,634,601	2,634,601
	100	263,630	263,631	263,633	263,631	263,630	263,633	263,631	263,634	263,630	263,632
	190	138,810	138,812	138,811	138,813	138,812	138,818	138,810	138,812	138,810	138,811
LL	10	2,783,955	2,783,955	2,783,954	2,783,955	2,783,953	2,783,959	2,783,955	2,783,955	2,783,955	2,783,955
	100	279,220	279,221	279,223	279,220	279,226	279,220	279,220	279,223	279,225	279,223
	190	147,310	147,310	147,314	147,310	147,315	147,313	147,311	147,313	147,310	147,313
LL-G	10	2,874,584	2,874,584	2,874,584	2,874,585	2,874,584	2,874,588	2,874,584	2,874,584	2,874,584	2,874,584
	100	276,791	276,793	276,791	276,791	276,796	276,795	276,791	276,790	276,791	276,792
	190	148,001	148,004	148,000	148,004	148,004	148,006	148,001	148,000	148,004	148,001
LLL	10	2,938,600	2,938,602	2,938,601	2,938,604	2,938,602	2,938,607	2,938,600	2,938,600	2,938,601	2,938,600
	100	293,820	293,821	293,820	293,823	293,821	293,823	293,820	2,938,255	293,821	293,821
	190	154,610	154,611	154,611	154,612	154,613	154,618	154,610	154,610	154,615	154,612
LLL-G	10	3,134,503	3,134,503	3,134,502	3,134,503	3,134,500	3,134,502	3,134,503	3,134,503	3,134,504	3,134,503
	100	312,860	312,861	312,861	312,860	312,862	312,864	312,860	312,863	312,861	312,860
	190	164,360	164,363	164,362	164,360	164,364	164,361	164,361	164,362	164,360	164,363

To demonstrate the fault localizer method, the proposed work carefully examines five different instances. As shown in Tables 4 and A9, Tables A10–A12, the maximum singular value of each faulty signal corresponding to the 19 separate fault locations throughout the length of the line is ascertained by utilizing a singular value to analyze the three-phase working signals to demonstrate this analytically.

**Table 4.** The maximum singular and its scaled values for LG fault at 19 locations.

Location (km)	The Max Singular Value	Max Scaled Singular Value
10	2,634,600	1
20	1,317,400	0.500038
30	878,350	0.33339
40	658,810	0.250061
50	527,090	0.200065
60	439,270	0.166731
70	376,540	0.142921
80	329,500	0.125066
90	292,910	0.111178
100	263,630	0.100065
110	239,680	0.090974
120	219,710	0.083394
130	202,820	0.076983
140	188,340	0.071487
150	175,800	0.066727
160	164,820	0.06256
170	155,130	0.058882
180	146,520	0.055614
190	138,810	0.052687

The maximum singular values obtained for the five faults in Tables 4 and A9, Tables A10–A12 are scaled in relation to the maximum values. For each phase independently, the curve fitting technique uses these 19 scaled S values of the faulty lines as training points.

The model is built using fault data from 19 locations, namely 10, 20, 30, 40, 50, 60, 70, 80, 90, 100, 110, 120, 130, 140, 150, 160, 170, 180, and 190 km, as previously discussed. Different curves are evaluated with these scaled singular value values to determine the optimal curve fitting method, which is discussed next.

### 5.3. Analysis of Different Fitness Models

Best-fit approaches are used to approximate the curvilinear nature. The least reduced chi-squared and maximum adjusted R-square criteria are used to choose the top five fittest models, with the best-fit model being selected among those:

$$\text{Fit 1 : } f(i) = a_0i + a_1 \quad (7)$$

$$\text{Fit 2 : } f(i) = a_0 + a_1i + a_2i^2 + a_3i^3 + a_4i^4 + a_5i^5 + a_6i^6 + a_7i^7 \quad (8)$$

$$\text{Fit 3 : } f(i) = a_1e^{ai} + a_2e^{bi} + a_3e^{ci} \quad (9)$$

$$\text{Fit 4 : } f(i) = a_1e^{-(i-b_1)/c_1} + a_2e^{-(i-b_2)/c_2} + a_3e^{-(i-b_3)/c_3} \quad (10)$$

$$\text{Fit 5 : } f(i) = a_0 + a_1e^{(-i/c_1)} + a_2e^{(-i/c_2)} + a_3e^{(-i/c_3)} \quad (11)$$

where  $a_0, a_1, c_1, a_2, c_2, a_3$  and  $c_3$  are of  $0.03435 \pm 9.00317 \times 10^{-4}$ ,  $2.33327 \pm 0.02426$ ,  $5.25993 \pm 0.09922$ ,  $0.7114 \pm 0.01814$ ,  $17.21614 \pm 0.451$ ,  $0.25131 \pm 0.00698$  and  $72.89877 \pm 1.96831$ , respectively. The fifth fitting formula has an R-Square (COD) = 1, R-squared value of 1, and Reduced Chi-Sqr =  $3.19786 \times 10^{-8}$ .

The five different fit models were progressively applied to the same set of maximum scaled singular values in order to determine which model provided the best fit with the least chi-squared and the highest adjusted R square. For the LG, LL, LL-G, LLL, and LLL-G faults, respectively, these best fit curves with the lowest reduced chi-squared and highest adjusted R-square. The best curve-fitting formula is accounted for in the fifth one. It is the most effective strategy for fault location determination. This last fitting expression employs an exponential decay with a third degree. The lowest possible error between the actual location and the predicted location is estimated using the proposed fitting formula at LG, LL, LL-G, LLL, and LLL-G faults, as depicted in Figure 6, Figure 7, Figure 8, Figure 9, and Figure 10, respectively. The difference between the predicted and real fault distances (P and A) was utilized to quantify this inaccuracy. This estimated error is equivalent to the algorithm's accuracy. As the distance deviation rises, the algorithm's accuracy falls. The overall accuracy is defined as the greatest estimate error throughout the whole length range of the line as well as for all conceivable fault types represented as a percentage of the total line length, C in Equation (12), and the average error (AE), is defined in Equation (13).

$$\text{error } (e) = \left| \frac{\text{predicted location(P)} - \text{actual location(A)}}{\text{total line length(C)}} \right| \times 100 \quad (12)$$

$$(AE) = \frac{\sum_{i=1}^n \text{error}}{n} \quad (13)$$

Tables 5–14 show the locations of five faults that were predicted based on current line data and fitted using various five-curve fitting methods. Furthermore, the average error (AE) and five different fault prediction errors using line current signals and various five curve fittings are shown in these tables. The proposed work produces a localization that is extremely accurate, with a maximum percentage error of 0.002% and an average percentage error for fault localization of just 0.0016%. The proposed approach is validated with other approaches, as shown in Table 15. Both the maximum and average percentage errors are computed and compared with literature work [9,11,12,35]. A comparison between the proposed work and that experimentally published is demonstrated. This comparison was made using the same data in the form of current signals. These simulated data are generated using ATP-EMTP that was tested with the mentioned methods on [9,11,12,35]. In addition, this data corresponds to changes in power system faults in a 200 km long, 500 kV Egyptian transmission line using sent end-line current signals. The proposed work is executed using a laptop with Intel(R) Core(TM) i7-10750H and a 2.59 GHz CPU. One of the main strengths of the suggested work is the ability to use it as a link between the nuclear power plant and the grid. Moreover, the proposed method is an effective fault

distance estimating method that might help to develop a reliable transient-based strategy for power system protection with minimal error.

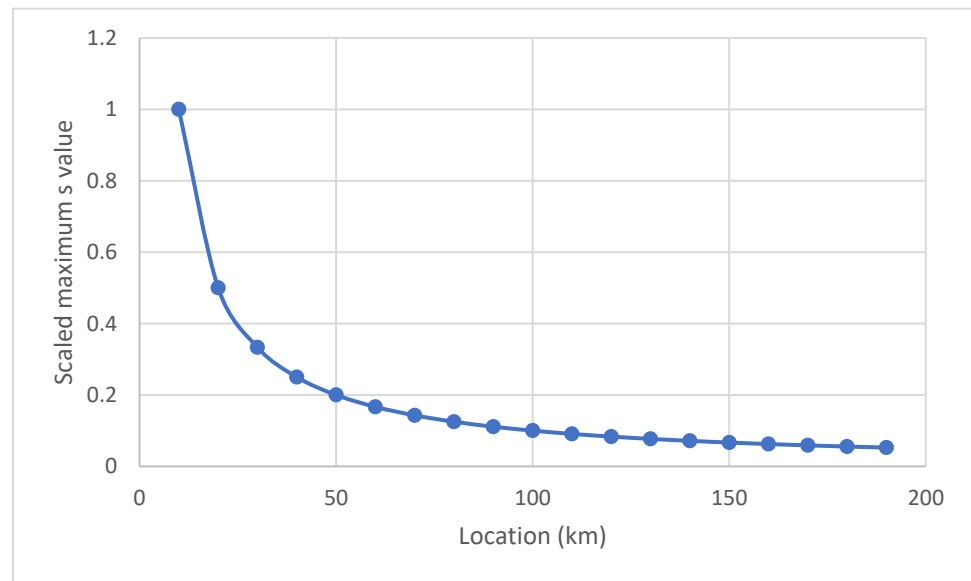


Figure 6. The best fitting curve at 19 fault locations for LG fault using scaled maximum singular value.

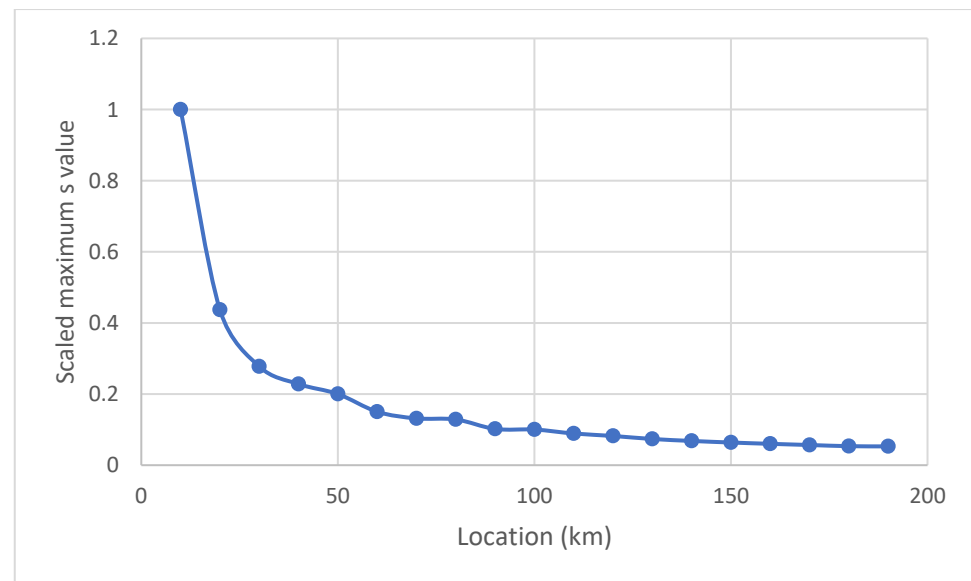


Figure 7. The best fitting curve at 19 fault locations for LL fault using scaled maximum singular value.

Table 5. Actual (A in km) and predicted (P in km) fault locations under LG fault scenario.

A (km)	10	30	50	70	90	100	120	140	160	180	190
P for Fit 1 (km)	10.5340	30.432	50.512	70.621	90.456	100.614	120.685	140.752	160.782	180.742	190.852
P for Fit 2 (km)	10.3211	30.312	50.468	70.425	90.562	100.568	120.536	140.568	160.311	180.541	190.752
P for Fit 3 (km)	10.1242	30.212	50.265	70.359	90.255	100.352	120.425	140.425	160.456	180.342	190.425
P for Fit 4 (km)	10.1181	30.102	50.120	70.130	90.125	100.129	120.235	140.254	160.352	180.213	190.246
P for Fit 5 (km)	10.0010	30.0024	50.002	70.0025	90.001	100.002	120.0022	140.002	160.003	180.003	190.003

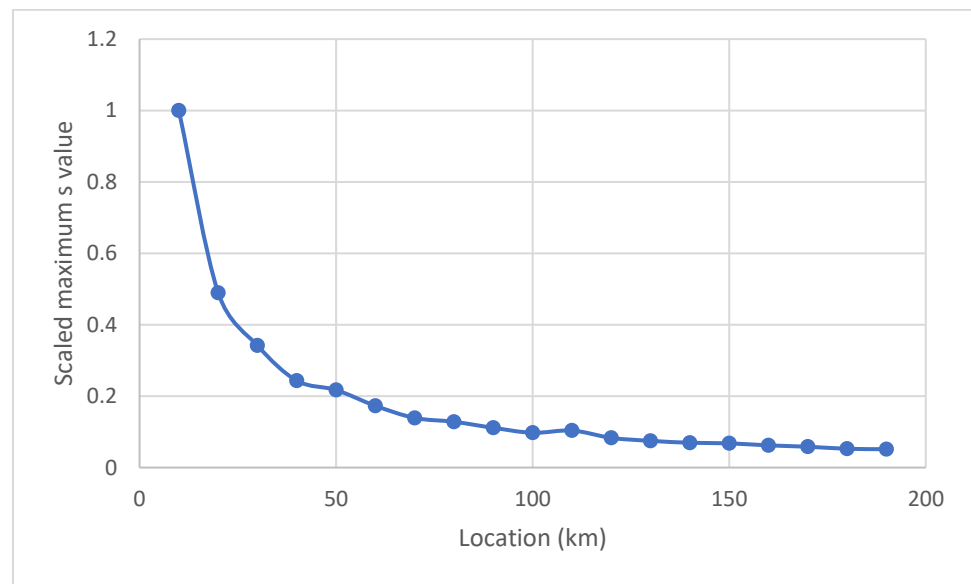


Figure 8. The best fitting curve at 19 fault locations for LL-G fault using scaled maximum singular value.

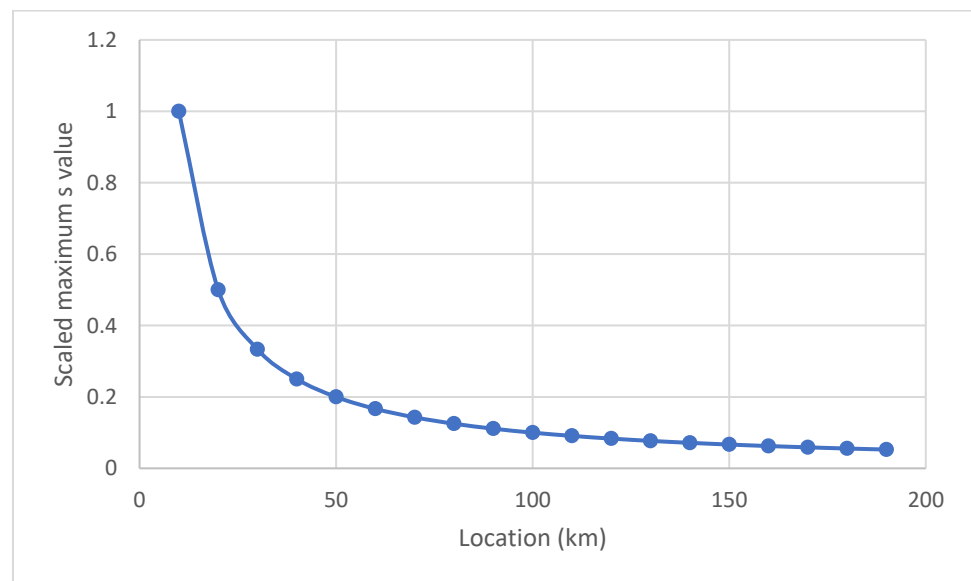


Figure 9. The best fitting curve at 19 fault locations for LLL fault using scaled maximum singular value.

Table 6. LG fault prediction error utilizing line current signals.

A (km)	10	30	50	70	90	100	120	140	160	180	190	AE (%)
error for Fit 1 (%)	0.267	0.216	0.256	0.3105	0.228	0.307	0.3425	0.376	0.391	0.394	0.426	0.319455
error for Fit 2 (%)	0.1605	0.156	0.234	0.2125	0.281	0.284	0.268	0.284	0.1555	0.2705	0.376	0.243818
error for Fit 3 (%)	0.062	0.106	0.1326	0.1795	0.1275	0.176	0.2125	0.2125	0.228	0.171	0.2125	0.165464
error for Fit 4 (%)	0.059	0.051	0.06	0.065	0.0625	0.0645	0.1175	0.127	0.176	0.1065	0.123	0.092000
error for Fit 5 (%)	0.0005	0.0012	0.001	0.00125	0.0005	0.001	0.0011	0.001	0.0015	0.0015	0.0015	0.001095

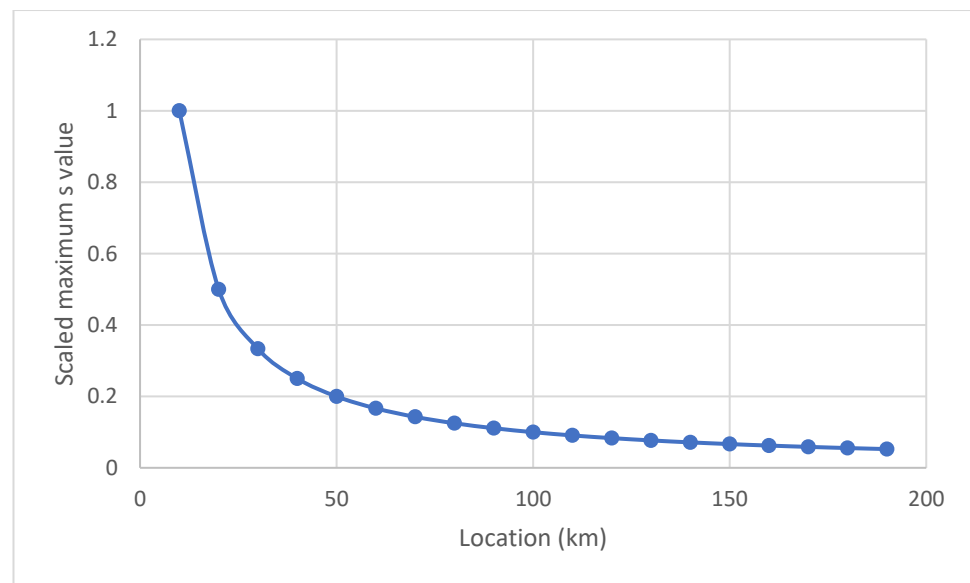


Figure 10. The best fitting curve at 19 fault locations for LLL-G fault using scaled maximum singular value.

Table 7. Actual (A in km) and predicted (P in km) fault locations under LL fault scenario.

A (km)	10	30	50	70	90	100	120	140	160	180	190
P for Fit 1 (km)	10.4820	30.523	50.623	70.528	90.711	100.692	120.695	140.723	160.722	180.823	190.722
P for Fit 2 (km)	10.2101	30.423	50.532	70.411	90.545	100.525	120.568	140.622	160.569	180.623	190.625
P for Fit 3 (km)	10.1512	30.198	50.225	70.325	90.456	100.352	120.458	140.352	160.355	180.456	190.425
P for Fit 4 (km)	10.1432	30.112	50.110	70.156	90.211	100.125	120.356	140.258	160.211	180.254	190.215
P for Fit 5 (km)	10.0011	30.0031	50.0023	70.002	90.0034	100.003	120.0021	140.0021	160.003	180.0031	190.0035

Table 8. LL fault prediction error.

A (km)	10	30	50	70	90	100	120	140	160	180	190	AE (%)
error for Fit 1 (%)	0.241	0.2615	0.3115	0.264	0.3555	0.346	0.3475	0.3615	0.361	0.4115	0.361	0.329273
error for Fit 2 (%)	0.10505	0.2115	0.266	0.2055	0.2725	0.2625	0.284	0.311	0.2845	0.3115	0.3125	0.256959
error for Fit 3 (%)	0.0756	0.099	0.1125	0.1625	0.228	0.176	0.229	0.176	0.1775	0.228	0.2125	0.1706
error for Fit 4 (%)	0.0716	0.056	0.055	0.078	0.1055	0.0625	0.178	0.129	0.1055	0.127	0.1075	0.097782
error for Fit 5 (%)	0.00055	0.00155	0.00115	0.001	0.0017	0.00125	0.00105	0.00105	0.0015	0.00155	0.00175	0.001282

Table 9. Actual (A in km) and predicted (P in km) fault locations under LL-G fault scenario.

A (km)	10	30	50	70	90	100	120	140	160	180	190
P for Fit 1 (km)	10.4910	30.725	50.561	70.568	90.774	100.621	120.685	140.711	160.799	180.759	190.812
P for Fit 2 (km)	10.3214	30.526	50.458	70.452	90.538	100.435	120.533	140.652	160.653	180.612	190.625
P for Fit 3 (km)	10.1245	30.3524	50.288	70.401	90.456	100.211	120.355	140.433	160.436	180.355	190.356
P for Fit 4 (km)	10.1395	30.182	50.124	70.128	90.364	100.178	120.244	140.311	160.235	180.215	190.282
P for Fit 5 (km)	10.0012	30.002	50.0032	70.0029	90.00296	100.003	120.002	140.0025	160.0028	180.003	190.0031

Table 10. LL-G fault prediction error.

A (km)	10	30	50	70	90	100	120	140	160	180	190	AE (%)
error for Fit 1 (%)	0.2455	0.3625	0.2805	0.284	0.387	0.3105	0.3425	0.3555	0.3995	0.3795	0.406	0.341182
error for Fit 2 (%)	0.1607	0.263	0.229	0.226	0.269	0.2175	0.2665	0.326	0.3265	0.306	0.3125	0.263882
error for Fit 3 (%)	0.06225	0.1762	0.144	0.2005	0.228	0.1055	0.1775	0.2165	0.218	0.1775	0.178	0.171268
error for Fit 4 (%)	0.06975	0.091	0.062	0.064	0.182	0.089	0.122	0.1555	0.1175	0.1075	0.141	0.109205
error for Fit 5 (%)	0.0006	0.001	0.0016	0.00145	0.00148	0.0015	0.001	0.00125	0.0014	0.0015	0.00155	0.001303

**Table 11.** Actual (A in km) and predicted (P in km) fault locations under LLL fault scenario.

A (km)	10	30	50	70	90	100	120	140	160	180	190
P for Fit 1 (km)	10.6212	30.526	50.785	70.752	90.744	100.511	120.752	140.811	160.823	180.835	190.851
P for Fit 2 (km)	10.4251	30.425	50.524	70.526	90.524	100.325	120.652	140.720	160.652	180.653	190.666
P for Fit 3 (km)	10.2520	30.236	50.411	70.456	90.411	100.235	120.532	140.511	160.328	180.422	190.513
P for Fit 4 (km)	10.1740	30.125	50.35	70.196	90.354	100.133	120.356	140.325	160.311	180.341	190.283
P for Fit 5 (km)	10.0021	30.0026	50.0029	70.003	90.0029	100.0035	120.003	140.003	160.0034	180.0032	190.0035

**Table 12.** LLL fault prediction error.

A (km)	10	30	50	70	90	100	120	140	160	180	190	AE (%)
error for Fit 1 (%)	0.3106	0.263	0.3925	0.376	0.372	0.2555	0.376	0.4055	0.4115	0.4175	0.4255	0.364145
error for Fit 2 (%)	0.2125	0.2125	0.262	0.263	0.262	0.1625	0.326	0.36	0.326	0.3265	0.333	0.276909
error for Fit 3 (%)	0.126	0.118	0.2055	0.228	0.2055	0.1175	0.266	0.2555	0.164	0.211	0.2565	0.195773
error for Fit 4 (%)	0.087	0.0625	0.175	0.098	0.177	0.0665	0.178	0.1625	0.1555	0.1705	0.1415	0.134000
error for Fit 5 (%)	0.00105	0.0013	0.00145	0.0015	0.00145	0.00175	0.0015	0.0015	0.0017	0.0016	0.00175	0.001505

**Table 13.** Actual (A in km) and predicted (P in km) fault locations under LLL-G fault scenario.

A (km)	10	30	50	70	90	100	120	140	160	180	190
P for Fit 1 (km)	10.6453	30.642	50.785	70.798	90.755	100.533	120.811	140.821	160.831	180.842	190.896
P for Fit 2 (km)	10.4932	30.498	50.429	70.652	90.623	100.325	120.652	140.711	160.599	180.711	190.756
P for Fit 3 (km)	10.4241	30.324	50.359	70.421	90.418	100.253	120.425	140.536	160.458	180.635	190.424
P for Fit 4 (km)	10.3242	30.110	50.192	70.199	90.212	100.172	120.352	140.324	160.352	180.361	190.213
P for Fit 5 (km)	10.0015	20.0032	50.003	70.0032	90.0036	100.003	120.0035	140.0034	160.0036	180.0035	190.004

**Table 14.** LLL-G fault prediction error.

A (km)	10	30	50	70	90	100	120	140	160	180	190	AE (%)
error for Fit 1 (%)	0.32265	0.321	0.3925	0.399	0.3775	0.2665	0.4055	0.4105	0.4155	0.421	0.4480	0.379968
error for Fit 2 (%)	0.2466	0.249	0.2145	0.326	0.3115	0.1625	0.326	0.355	0.2995	0.3555	0.3780	0.293100
error for Fit 3 (%)	0.21205	0.162	0.1795	0.2105	0.209	0.1265	0.2125	0.268	0.229	0.3175	0.2120	0.212595
error for Fit 4 (%)	0.1621	0.055	0.096	0.0995	0.106	0.086	0.176	0.162	0.176	0.1805	0.1065	0.127782
error for Fit 5 (%)	0.00075	0.0016	0.0015	0.0016	0.0018	0.0015	0.00175	0.0017	0.0018	0.00175	<b>0.0020</b>	<b>0.001614</b>

**Table 15.** Validation of the proposed algorithm compared to literature work in [9,11,12,35].

Literature & Proposed Work	Methods	Maximum Percentage Error (%)	Average Percentage Error (%)
[9]	PCA	0.3217	0.1921
[11]	CNN	0.0497	0.03670
[12]	ANN	0.4522	0.2375
[35]	MCSVM	0.0832	0.06790
The Proposed	FRFT-SVD	<b>0.0020</b>	<b>0.001614</b>

## 6. Conclusions

The FRFT-SVD method, which is very effective, precise, and straightforward, was used to develop the localizer model. Here is a practical power system protection approach for long-distance power system issue prediction for a 500 kV, 50 Hz, 200 km overhead transmission line. FRFT-SVD was used to develop the suggested protective mechanism. Using the best-fit curve method, sending end current signals are evaluated after being subjected to FRFT-SVD analysis to obtain fault characteristics expressed in terms of the highest S value. Only around 0.001614% of the typical scheme is inaccurate. The lowest estimate for an LLL-G defect was 0.002%, which is also quite precise for a 200-km long line. This paper aims to provide a technique for predicting the location of faults using

curve fitting analysis and FRFT-SVD. For this reason, the analysis makes use of a variety of noise, inception angle, and fault resistance variables. The proposed method may prove to be an effective way to gauge how far a problem would spread, which might be useful in creating a dependable transient-based power system security strategy. In future work, we will implement the new model in hardware and apply it in real systems with different configurations.

**Author Contributions:** Conceptualization, M.H.S., M.M.F. and A.S.; Methodology, M.H.S., M.M.F. and A.S.; Software, M.H.S., M.M.F. and A.S.; Validation, M.H.S., M.M.F. and A.S.; Formal analysis, M.H.S., M.M.F. and A.S.; Investigation, M.H.S., M.M.F. and A.S.; Writing—original draft, M.H.S., M.M.F. and A.S.; Writing—review & editing, M.H.S., M.M.F. and A.S.; Visualization, M.H.S., M.M.F. and A.S. All authors have read and agreed to the published version of the manuscript.

**Funding:** This research received no external funding.

**Data Availability Statement:** Data is available upon a request to the authors.

**Conflicts of Interest:** The authors declare no conflict of interest.

## Appendix A

Here, an appendix is presented for several fault results. These faults are LL fault, LL-G fault, LLL fault and LLL-G fault. The max singular values of FRFT-SVD results at various SNRs for direct and filtered signals under LL fault, LL-G fault, LLL fault, and LLL-G fault scenarios are depicted in Tables A1–A4, respectively. The results in these tables confirm that the variations of SNR values have no impact on the max singular value of the FRFT-SVD.

**Table A1.** Max singular value of FRFT-SVD results at various SNRs for direct and filtered signals under LL fault scenario.

Location (km)	SNR = 15 dB		SNR = 20 dB		SNR = 25 dB		SNR = 30 dB	
	Direct	Filtered	Direct	Filtered	Direct	Filtered	Direct	Filtered
10	2,783,955	2,783,954	2,783,952	2,783,952	2,783,953	2,783,951	2,783,952	2,783,951
20	1,216,531	1,216,532	1,216,530	1,216,533	1,216,532	1,216,531	1,216,531	1,216,532
30	773,253	773,252	773,250	773,253	773,253	773,253	773,253	773,253
40	635,422	635,421	635,422	635,424	635,422	635,422	635,422	635,420
50	557,560	557,565	557,561	557,563	557,566	557,562	557,560	557,561
60	418,326	418,323	418,321	418,322	418,326	418,326	418,326	4,183,262
70	366,330	366,331	366,333	366,330	366,330	366,330	366,330	366,330
80	358,422	358,421	358,420	358,422	358,423	358,424	358,420	358,422
90	283,721	283,722	283,721	283,723	283,720	283,721	283,720	283,721
100	279,220	279,221	279,223	279,222	279,224	279,221	279,220	279,221
110	248,230	248,231	248,230	248,231	248,230	248,232	248,231	248,230
120	228,880	228,882	228,882	228,881	228,880	228,883	228,880	228,881
130	205,200	205,201	205,201	205,200	205,200	205,200	205,200	205,200
140	189,931	189,930	189,932	189,931	189,932	189,933	189,931	189,930
150	177,536	177,534	177,531	177,533	177,536	177,531	177,534	177,532
160	167,320	167,322	167,320	167,320	167,320	167,322	167,321	167,320
170	158,223	158,220	158,223	158,223	158,223	158,223	158,223	158,223
180	148,880	248,231	248,230	248,230	248,230	248,230	248,230	248,230
190	147,310	147,313	147,311	147,313	147,311	147,315	147,310	147,313

**Table A2.** Max singular value of FRFT-SVD results at various SNRs for direct and filtered signals under LL-G fault scenario.

Location (km)	SNR = 15 dB		SNR = 20 dB		SNR = 25 dB		SNR = 30 dB	
	Direct	Filtered	Direct	Filtered	Direct	Filtered	Direct	Filtered
10	2,874,584	2,874,585	2,874,580	2,874,581	2,874,582	2,874,583	2,874,584	2,874,585
20	1,317,210	1,317,213	1,317,213	1,317,210	1,317,211	1,317,210	1,317,212	1,317,210
30	782,500	782,501	782,502	782,501	782,500	782,500	782,502	782,503
40	662,530	662,532	662,533	662,530	662,533	662,530	662,531	662,530
50	624,440	624,442	624,442	624,443	624,441	624,445	624,440	624,442
60	437,210	437,211	437,210	437,210	437,212	437,212	437,210	437,213
70	382,501	382,503	382,502	382,500	382,503	382,501	382,502	382,501
80	368,521	368,522	368,520	368,521	368,520	368,521	368,520	368,521
90	288,823	288,820	288,821	288,822	288,823	288,820	288,823	288,821
100	276,791	276,792	276,790	276,792	276,793	276,790	276,790	276,791
110	241,230	241,233	241,232	241,230	241,232	241,230	241,231	241,230
120	228,880	228,883	228,882	228,881	228,883	228,883	228,882	228,881
130	215,200	215,201	215,202	215,204	215,201	215,202	215,203	215,200
140	187,011	187,013	187,013	187,010	187,014	187,011	187,010	187,012
150	195,012	195,010	195,010	195,011	195,012	195,013	195,012	195,010
160	168,432	168,430	168,431	168,432	168,430	168,432	168,433	168,431
170	157,882	157,883	157,880	157,882	157,882	157,881	157,883	157,881
180	151,230	151,231	151,230	151,233	151,230	151,232	151,230	151,232
190	148,001	148,003	148,001	148,002	148,003	148,002	148,000	148,001

**Table A3.** Max singular value of FRFT-SVD results at various SNRs for direct and filtered signals under LLL fault scenario.

Location (km)	SNR = 15 dB		SNR = 20 dB		SNR = 25 dB		SNR = 30 dB	
	Direct	Filtered	Direct	Filtered	Direct	Filtered	Direct	Filtered
10	2,938,600	2,938,602	2,938,601	2,938,602	2,938,602	2,938,601	2,938,603	2,938,602
20	1,469,300	14,693,033	1,469,303	1,469,302	1,469,301	1,469,302	1,469,303	1,469,301
30	979,520	979,523	979,522	9,795,210	979,521	979,521	979,522	979,521
40	734,640	734,643	734,641	734,642	734,642	734,641	734,642	734,640
50	587,690	587,694	587,691	587,691	587,691	587,691	587,692	587,691
60	489,740	489,745	489,742	489,741	489,742	489,742	489,741	489,740
70	419,770	419,772	419,771	419,772	419,771	419,772	419,771	419,770
80	367,300	367,305	367,303	367,301	367,301	367,302	367,300	367,301
90	326,480	326,482	326,481	326,482	326,481	326,481	326,481	326,480
100	293,820	293,823	293,821	293,821	293,821	293,821	293,820	293,821
110	267,110	267,113	267,113	267,111	267,111	267,113	267,110	267,110
120	244,850	244,852	244,852	244,851	244,851	244,852	244,852	244,852
130	226,010	226,013	226,013	226,012	226,011	226,011	226,010	226,011
140	209,860	209,862	209,861	209,861	209,862	209,861	209,861	209,862
150	195,870	195,873	195,871	195,871	195,873	195,871	195,871	195,870
160	183,620	183,621	183,622	183,621	183,622	183,621	183,621	183,622
170	172,820	172,822	172,823	172,822	172,821	172,822	172,822	172,820
180	163,210	163,212	163,213	163,211	163,212	163,210	163,210	163,211
190	154,610	154,615	154,612	154,611	154,613	154,611	154,612	154,611

**Table A4.** Max singular value of FRFT-SVD results at various SNRs for direct and filtered signals under LLL-G fault scenario.

Location (km)	SNR = 15 dB		SNR = 20 dB		SNR = 25 dB		SNR = 30 dB	
	Direct	Filtered	Direct	Filtered	Direct	Filtered	Direct	Filtered
10	3,134,503	3,134,501	3,134,502	3,134,501	3,134,500	3,134,501	3,134,503	3,134,501
20	1,566,902	1,566,900	1,566,901	1,566,901	1,566,901	1,566,902	1,566,903	1,566,900
30	1,044,400	1,044,401	1,044,402	1,044,402	1,044,401	1,044,401	1,044,402	1,044,400
40	783,140	783,142	783,142	783,142	783,142	783,140	783,143	783,141
50	626,370	626,373	626,373	626,372	626,372	626,372	626,373	626,372
60	521,870	521,875	521,871	521,872	521,872	521,871	521,872	521,871
70	447,230	447,231	447,231	447,232	447,231	447,231	447,231	447,231
80	391,250	391,251	391,252	391,253	391,251	391,252	391,250	391,251
90	347,700	347,701	347,702	347,703	347,700	347,701	347,701	347,702
100	312,860	312,862	312,863	312,861	312,862	312,862	312,861	312,861
110	284,360	284,362	284,362	284,361	284,362	284,362	284,362	284,361
120	260,620	260,621	260,621	260,622	260,623	260,623	260,622	260,623
130	240,522	240,521	240,521	240,521	240,522	240,523	240,522	240,523
140	223,290	223,293	223,292	223,293	223,291	223,293	223,292	223,292
150	208,361	208,360	208,364	208,363	208,362	208,361	208,362	208,362
160	195,300	195,301	195,304	195,302	195,303	195,301	195,301	195,301
170	183,770	183,770	183,773	183,771	183,772	183,771	183,771	183,772
180	173,520	173,521	173,522	173,522	173,523	173,521	173,522	173,522
190	164,360	164,363	164,362	164,361	164,361	164,362	164,361	164,361

## Appendix B

Influences of both inception angles and fault resistances on the Max singular values of FRFT-SVD are declared in Appendix B. The considered inception angles are  $0^\circ$ ,  $45^\circ$ ,  $90^\circ$ ,  $135^\circ$ , and  $180^\circ$ . However, the fault resistances accounted for  $50 \Omega$ ,  $100 \Omega$ ,  $150 \Omega$  and  $200 \Omega$ . The results of max singular values of FRFT-SVD for direct and filtered current signals at various faults and inception angles with fault resistances  $50 \Omega$ ,  $100 \Omega$ ,  $150 \Omega$  and  $200 \Omega$  are respectively shown in Tables A5–A8. These results conclude that both inception angles and fault resistances do not affect the proposed algorithm's performance.

**Table A5.** Max singular values of FRFT-SVD results for direct and filtered current signals at various faults and inception angles with  $R = 50 \Omega$ .

Inception Angle		$0^\circ$		$45^\circ$		$90^\circ$		$135^\circ$		$180^\circ$	
Faults	Location (km)	Direct	Filtered	Direct	Filtered	Direct	Filtered	Direct	Filtered	Direct	Filtered
LG	10	2,634,601	2,634,603	2,634,601	2,634,601	2,634,604	2,634,601	2,634,603	2,634,601	2,634,601	2,634,601
	100	263,632	263,631	263,630	263,633	263,631	263,630	263,631	263,631	263,630	263,632
	190	138,810	138,814	138,810	138,811	138,815	138,812	138,812	138,810	138,813	138,810
LL	10	2,783,953	2,783,952	2,783,955	2,783,952	2,783,958	2,783,957	2,783,955	2,783,952	2,783,955	2,783,953
	100	279,221	279,220	279,223	279,221	279,225	279,221	279,222	279,220	279,223	279,221
	190	147,310	147,311	147,314	147,310	147,312	147,316	147,311	147,310	147,314	147,312
LL-G	10	2,874,584	2,874,585	2,874,586	2,874,584	2,874,588	2,874,580	2,874,581	2,874,584	2,874,583	2,874,580
	100	276,791	276,793	276,791	276,792	276,795	276,793	276,790	276,791	276,790	276,792
	190	148,000	148,004	148,001	148,005	148,003	148,007	148,002	148,001	148,003	148,001
LLL	10	2,938,601	2,938,603	2,938,600	2,938,600	2,938,602	2,938,605	2,938,601	2,938,600	2,938,600	2,938,600
	100	293,822	293,821	293,823	293,820	293,821	293,825	293,822	293,824	293,820	293,823
	190	154,610	154,612	154,610	154,610	154,613	154,616	154,613	154,611	154,613	154,611
LLL-G	10	3,134,503	3,134,502	3,134,503	3,134,503	3,134,503	3,134,500	3,134,503	3,134,503	3,134,503	3,134,503
	100	312,864	312,860	312,860	312,860	312,862	312,867	312,862	312,860	312,863	312,862
	190	164,364	164,360	164,360	164,360	164,361	164,368	164,361	164,363	164,360	164,363

**Table A6.** Max singular values of FRFT-SVD results for direct and filtered current signals at various faults and inception angles with  $R = 100 \Omega$ .

Inception Angle		0°		45°		90°		135°		180°	
Faults	Location (km)	Direct	Filtered								
LG	10	2,634,602	2,634,601	2,634,600	2,634,603	2,634,602	2,634,605	2,634,601	2,634,603	2,634,604	2,634,603
	100	263,633	263,631	263,632	263,635	263,632	263,636	263,633	263,634	263,631	263,632
	190	138,811	138,812	138,811	138,814	138,812	138,816	138,810	138,812	138,811	138,813
LL	10	2,783,951	2,783,953	2,783,952	2,783,951	2,783,959	2,783,950	2,783,952	2,783,954	2,783,955	2,783,956
	100	279,222	279,220	279,222	279,224	279,225	279,227	279,222	279,221	279,220	279,221
	190	147,313	147,310	147,313	147,312	147,313	147,318	147,311	147,310	147,313	147,314
LL-G	10	2,874,584	2,874,582	2,874,583	2,874,581	2,874,587	2,874,580	2,874,583	2,874,584	2,874,581	2,874,580
	100	276,792	276,791	276,790	276,791	276,797	276,795	276,794	276,791	276,790	276,792
	190	148,001	148,004	148,002	148,005	148,009	148,002	148,003	148,005	148,004	148,002
LLL	10	2,938,602	2,938,603	2,938,602	2,938,602	2,938,605	2,938,607	2,938,601	2,938,601	2,938,602	2,938,603
	100	293,821	293,824	29,382	293,821	293,825	293,828	293,825	293,820	293,822	293,821
	190	154,613	154,611	154,613	154,614	154,614	154,616	154,612	154,615	154,612	154,614
LLL-G	10	3,134,505	3,134,503	3,134,505	3,134,505	3,134,502	3,134,501	3,134,502	3,134,503	3,134,502	3,134,501
	100	312,861	312,860	312,863	312,864	312,865	312,869	312,864	3,128,610	312,861	312,863
	190	164,362	164,365	164,363	164,362	164,366	164,361	164,364	164,362	164,362	164,361

**Table A7.** Max singular values of FRFT-SVD results for direct and filtered current signals at various faults and inception angles with  $R = 150 \Omega$ .

Inception Angle		0°		45°		90°		135°		180°	
Faults	Location (km)	Direct	Filtered	Direct	Filtered	Direct	Filtered	Direct	Filtered	Direct	Filtered
LG	10	2,634,601	2,634,605	2,634,602	2,634,604	2,634,604	2,634,601	2,634,604	2,634,604	2,634,604	2,634,605
	100	263,631	263,632	263,631	263,632	263,635	263,638	263,635	263,631	263,631	263,631
	190	138,813	138,810	138,813	138,815	138,818	138,817	138,812	138,812	138,811	138,815
LL	10	2,783,951	2,783,954	2,783,954	2,783,955	2,783,954	2,783,950	2,783,954	2,783,952	2,783,954	2,783,955
	100	279,222	279,221	279,224	279,223	279,223	279,220	279,225	279,223	279,222	279,221
	190	147,313	147,312	147,318	147,312	147,315	147,315	147,314	147,311	147,312	147,313
LL-G	10	2,874,581	28,745,834	2,874,584	2,874,585	2,874,588	2,874,585	2,874,585	2,874,581	2,874,583	2,874,582
	100	276,791	276,792	276,795	276,793	276,795	276,794	276,792	276,792	276,790	276,791
	190	148,003	148,005	148,001	148,005	148,008	148,007	148,003	148,000	148,002	148,001
LLL	10	2,938,603	2,938,604	2,938,600	2,938,605	2,938,607	2,938,609	2,938,603	2,938,602	2,938,602	2,938,601
	100	293,822	293,821	293,820	293,823	293,826	293,824	293,824	293,821	293,821	293,823
	190	154,611	154,610	154,610	154,610	154,610	154,612	154,612	154,613	154,611	154,612
LLL-G	10	3,134,501	3,134,503	3,134,504	3,134,503	3,134,502	3,134,503	3,134,507	3,134,505	3,134,503	3,134,502
	100	312,863	312,860	312,864	312,862	312,866	312,865	312,864	312,860	312,861	312,864
	190	164,364	164,362	164,363	164,364	164,367	164,365	164,365	164,360	164,363	164,362

**Table A8.** Max singular values of FRFT-SVD results for direct and filtered current signals at various faults and inception angles with  $R = 200 \Omega$ .

Inception Angle		0°		45°		90°		135°		180°	
Faults	Location (km)	Direct	Filtered								
LG	10	2,634,601	2,634,603	2,634,602	2,634,601	2,634,608	2,634,603	2,634,604	2,634,601	2,634,601	2,634,602
	100	263,631	263,632	263,632	263,634	263,636	263,635	263,632	263,635	263,633	263,631
	190	138,814	138,811	138,813	138,810	138,817	138,812	138,812	138,814	138,811	138,810
LL	10	2,783,953	2,783,953	2,783,955	2,783,954	2,783,950	2,783,955	2,783,955	2,783,955	2,783,955	2,783,953
	100	279,222	279,223	279,222	279,225	279,226	279,223	279,223	279,222	279,222	279,220
	190	147,313	147,311	147,315	147,313	147,317	147,314	147,310	147,315	147,314	147,314
LL-G	10	2,874,585	2,874,581	2,874,584	2,874,584	2,874,589	2,874,584	2,874,584	2,874,584	2,874,587	2,874,584
	100	276,790	276,792	276,791	276,791	276,798	276,793	276,791	276,793	276,798	276,793
	190	148,000	148,001	148,003	148,004	148,008	148,001	148,005	148,001	148,001	148,005
LLL	10	2,938,603	2,938,605	2,938,604	2,938,605	2,938,607	2,938,604	2,938,602	2,938,602	2,938,604	2,938,603
	100	293,820	293,823	293,820	293,822	293,820	293,823	293,823	293,820	293,820	293,822
	190	154,614	154,610	154,611	154,610	154,615	154,612	154,610	154,614	154,614	154,611
LLL-G	10	3,134,503	3,134,501	3,134,503	3,134,503	3,134,503	3,134,501	3,134,503	3,134,503	3,134,505	3,134,502
	100	312,862	312,864	312,864	312,861	312,863	312,862	312,863	312,862	312,864	312,861
	190	164,362	164,361	164,365	164,364	164,369	164,362	164,360	164,363	164,361	164,361

### Appendix C

In this appendix, the maximum singular and its scaled values of FRFT-SVD at 19 different location values are investigated. These values are utilized for curve fitting to get a proper formula of fault locations. Accordingly, the maximum singular and its scaled values at 19 locations for LL fault, LL-G fault, LLL fault and LLL-G fault are declared in Tables A9–A12, respectively.

**Table A9.** The maximum singular and its scaled values for LL fault at 19 locations.

Location (km)	Max Singular Value	Max Scaled Singular Value
10	2,783,955	1
20	1,392,500	0.436979
30	928,640	0.277753
40	696,720	0.228244
50	557,560	0.200276
60	464,780	0.150263
70	398,510	0.131586
80	348,810	0.128746
90	310,150	0.101913
100	279,220	0.100296
110	253,910	0.089165
120	232,820	0.082214
130	214,970	0.073708
140	199,670	0.068223
150	186,410	0.063771
160	174,800	0.060102
170	164,560	0.056834
180	155,460	0.053478
190	147,310	0.052914

**Table A10.** The maximum singular and its scaled values for LL-G fault at 19 locations.

Location (km)	Max Singular Value	Max Scaled Singular Value
10	2,874,584	1
20	1,407,210	0.489535
30	982,500	0.341789
40	699,530	0.24335
50	624,440	0.217228
60	497,210	0.172968
70	399,501	0.138977
80	368,521	0.1282
90	320,150	0.111373
100	279,991	0.097402
110	298,230	0.103747
120	238,880	0.083101
130	215,200	0.074863
140	199,711	0.069475
150	195,012	0.06784
160	178,432	0.062072
170	167,882	0.058402
180	151,230	0.052609
190	148,001	0.051486

**Table A11.** The maximum singular and its scaled values for LLL fault at 19 locations.

Location (km)	Max Singular Value	Max Scaled Singular Value
10	2,938,600	1
20	1,469,300	0.500000
30	979,520	0.333329
40	734,640	0.249997
50	587,690	0.19999
60	489,740	0.166658
70	419,770	0.142847
80	367,300	0.124991
90	326,480	0.111101
100	293,820	0.099986
110	267,110	0.090897
120	244,850	0.083322
130	226,010	0.076911
140	209,860	0.071415
150	195,870	0.066654
160	183,620	0.062486
170	172,820	0.05881
180	163,210	0.05554
190	154,610	0.052613

**Table A12.** The maximum singular and its scaled values for LLL-G fault at 19 locations.

Location (km)	Max Singular Value	Max Scaled Singular Value
10	3,134,500	1
20	1,566,900	0.499888
30	1,044,400	0.333195
40	783,140	0.249845
50	626,370	0.199831
60	521,870	0.166492
70	447,230	0.14268
80	391,250	0.124821
90	347,700	0.110927
100	312,860	0.099812
110	284,360	0.090719
120	260,620	0.083146
130	240,520	0.076733
140	223,290	0.071236
150	208,360	0.066473
160	195,300	0.062307
170	183,770	0.058628
180	173,520	0.055358
190	164,360	0.052436

## References

- Gaur, V.K.; Bhalja, B.R.; Kezunovic, M. Novel Fault Distance Estimation Method for Three-Terminal Transmission Line. *IEEE Trans. Power Deliv.* **2021**, *36*, 406–417. [\[CrossRef\]](#)
- Hashemian, S.M.; Hashemian, S.N.; Gholipour, M. Unsynchronized parameter free fault location scheme for hybrid transmission line. *Electr. Power Syst. Res.* **2021**, *192*, 106982. [\[CrossRef\]](#)
- Liang, R.; Peng, N.; Zhou, L.; Meng, X.; Hu, Y.; Shen, Y.; Xue, X. Fault location method in power network by applying accurate information of arrival time differences of modal traveling waves. *IEEE Trans. Ind. Inf.* **2020**, *16*, 3124–3132. [\[CrossRef\]](#)
- Abd el-Ghany, H.A.; Azmy, A.M.; Abeid, A.M. A general travelling-wavebased scheme for locating simultaneous faults in transmission lines. *IEEE Trans. Power Deliv.* **2020**, *35*, 130–139. [\[CrossRef\]](#)
- Lopes, F.; Dantas, K.; Silva, K.; Costa, F.B. Accurate Two-Terminal Transmission Line Fault Location Using Traveling Waves. *IEEE Trans. Power Deliv.* **2018**, *33*, 873–880. [\[CrossRef\]](#)
- Ezquerro, J.; Valverde, V.; Mazón, A.; Zamora, I.; Zamora, J. Field programmable gate array implementation of a fault location system in transmission lines based on artificial neural networks. *IET Gener. Transm. Distrib.* **2011**, *5*, 191–198. [\[CrossRef\]](#)
- Farshad, M.; Sadeh, J. Transmission line fault location using hybrid wavelet-Prony method and relief algorithm. *Int. J. Electr. Power Energy Syst.* **2014**, *61*, 127–136. [\[CrossRef\]](#)
- Rezaei, D.; Gholipour, M.; Parvaresh, F. A new traveling-wave detection method for fault location based on two sequential sliding windows and curve fitting. *IET Gener. Transm. Distrib.* **2022**, *16*, 3333–3348. [\[CrossRef\]](#)
- Mukherjee, A.; Kundu, P.K.; Das, A. Transmission Line Fault Location Using PCA-Based Best-Fit Curve Analysis. *J. Inst. Eng. (India) Ser. B* **2021**, *102*, 339–350. [\[CrossRef\]](#)
- Mukherjee, A.; Kundu, P.K.; Das, A. Classification and localization of transmission line faults using curve fitting technique with Principal component analysis features. *Electr. Eng.* **2021**, *103*, 2929–2944. [\[CrossRef\]](#)
- Said, A.; Hashima, S.; Fouda, M.M.; Saad, M.H. Deep Learning-Based Fault Classification and Location for Underground Power Cable of Nuclear Facilities. *IEEE Access* **2022**, *10*, 70126–70142. [\[CrossRef\]](#)
- Roy, Nabamita, and Kesab Bhattacharya. Detection, classification, and estimation of fault location on an overhead transmission line using S-transform and neural network. *Electr. Power Compon. Syst.* **2015**, *43*, 461–472. [\[CrossRef\]](#)
- Akmaz, D.; Mamiş, M.S.; Arkan, M.; Tağluk, M.E. Transmission line fault location using traveling wave frequencies and extreme learning machine. *Electr. Power Syst. Res.* **2018**, *155*, 1–7. [\[CrossRef\]](#)
- Rao, H.V.G.; Prabhu, N.; Mala, R.C. Wavelet transform-based protection of transmission line incorporating SSSC with energy storage device. *Electr. Eng.* **2020**, *102*, 1593–1604. [\[CrossRef\]](#)
- Yadav, A.; Swetapadma, A. Enhancing the performance of transmission line directional relaying, fault classification and fault location schemes using fuzzy inference system. *IET Gener. Transm. Distrib.* **2015**, *9*, 580–591. [\[CrossRef\]](#)
- Reddy, M.J.B.; Mohanta, D.K. A wavelet-fuzzy combined approach for classification and location of transmission line faults. *Int. J. Electr. Power Energy Syst.* **2007**, *29*, 669–678. [\[CrossRef\]](#)
- Meyur, R.; Pal, D.; Sundaravaradan, N.; Rajaraman, P.; Srinivas, K.; Reddy, M.J.B.; Mohanta, D. A wavelet-adaptive network based fuzzy inference system for location of faults in parallel transmission lines. In Proceedings of the 2016 IEEE International

- Conference on Power Electronics, Drives and Energy Systems (PEDES), Trivandrum, India, 14–17 December 2016; IEEE: New York, NY, USA, 2016. [\[CrossRef\]](#)
18. Salat, R.; Osowski, S. Accurate Fault Location in the Power Transmission Line Using Support Vector Machine Approach. *IEEE Trans. Power Syst.* **2004**, *19*, 979–986. [\[CrossRef\]](#)
  19. Chothani, N.G.; Bhalja, B.; Parikh, U.B. New fault zone identification scheme for busbar using support vector machine. *IET Gener. Transm. Distrib.* **2011**, *5*, 1073–1079. [\[CrossRef\]](#)
  20. Reddy, M.J.B.; Gopakumar, P.; Mohanta, D. A novel transmission line protection using DOST and SVM. *Eng. Sci. Technol. Int. J.* **2016**, *19*, 1027–1039. [\[CrossRef\]](#)
  21. Bhalja, B.; Maheshwari, R.P. Wavelet-based Fault Classification Scheme for a Transmission Line Using a Support Vector Machine. *Electr. Power Compon. Syst.* **2008**, *36*, 1017–1030. [\[CrossRef\]](#)
  22. Jafarian, P.; Sanaye-Pasand, M. High-Frequency Transients-Based Protection of Multiterminal Transmission Lines Using the SVM Technique. *IEEE Trans. Power Deliv.* **2012**, *28*, 188–196. [\[CrossRef\]](#)
  23. Gaur, V.K.; Bhalja, B. A new faulty section identification and fault localization technique for three-terminal transmission line. *Int. J. Electr. Power Energy Syst.* **2017**, *93*, 216–227. [\[CrossRef\]](#)
  24. Kazim, M.; Khawaja, A.H.; Zabit, U.; Huang, Q. Fault detection and localization for overhead 11-kV distribution lines with magnetic measurements. *IEEE Trans. Instrum. Meas.* **2019**, *69*, 2028–2038. [\[CrossRef\]](#)
  25. Godse, R.; Bhat, S. Mathematical Morphology-Based Feature-Extraction Technique for Detection and Classification of Faults on Power Transmission Line. *IEEE Access* **2020**, *8*, 38459–38471. [\[CrossRef\]](#)
  26. Fan, R.; Liu, Y.; Huang, R.; Diao, R.; Wang, S. Precise Fault Location on Transmission Lines Using Ensemble Kalman Filter. *IEEE Trans. Power Deliv.* **2018**, *33*, 3252–3255. [\[CrossRef\]](#)
  27. Jiao, Z.; Wu, R. A new method to improve fault location accuracy in transmission line based on fuzzy multi-sensor data fusion. *IEEE Trans. Smart Grid* **2018**, *10*, 4211–4220. [\[CrossRef\]](#)
  28. Palangar, M.F.; Amin, U.; Bakhshayesh, H.; Ahmad, G.; Abu-Siada, A.; Mirzaie, M. Identification of Composite Insulator Criticality Based on a New Leakage Current Diagnostic Index. *IEEE Trans. Instrum. Meas.* **2021**, *70*, 9004110. [\[CrossRef\]](#)
  29. Faramarzipalangar, M.; Mohseni, S.; Mirzaie, M.; Mahmoudi, A. Designing an Automatic Detector Device to Diagnose Insulator State on Overhead Distribution Lines. *IEEE Trans. Ind. Inform.* **2022**, *18*, 1072–1082. [\[CrossRef\]](#)
  30. Palangar, M.F.; Mohseni, S.; Abu-Siada, S.M.A.; Mirzaie, M. Online Condition Monitoring of Overhead Insulators Using Pattern Recognition Algorithm. *IEEE Trans. Instrum. Meas.* **2022**, *71*, 6007111. [\[CrossRef\]](#)
  31. Said, A.; Anane, Z. Corona lightning overvoltage analysis for a 500 kV hybrid line. *IET Gener. Transm. Distrib.* **2019**, *14*, 532–541. [\[CrossRef\]](#)
  32. Said, A. Analysis of 500 kV OHTL polluted insulator string behavior during lightning strokes. *Int. J. Electr. Power Energy Syst.* **2018**, *95*, 405–416. [\[CrossRef\]](#)
  33. Ozaktas, H.; Arikan, O.; Kutay, M.; Bozdag, G. Digital computation of the fractional Fourier transform. *IEEE Trans. Signal Process.* **1996**, *44*, 2141–2150. [\[CrossRef\]](#)
  34. Krishna, B.T. Fractional Fourier transform. In Proceedings of the International Conference on Advances in Computing, Communications and Informatics (ICACCI'12), Chennai, India, 3–5 August 2012; ACM Press: New York, NY, USA, 2012.
  35. Saad, M.H.; Said, A. Machine learning-based fault diagnosis for research nuclear reactor medium voltage power cables in fraction Fourier domain. *Electr. Eng.* **2022**, 1–18. [\[CrossRef\]](#)

**Disclaimer/Publisher’s Note:** The statements, opinions and data contained in all publications are solely those of the individual author(s) and contributor(s) and not of MDPI and/or the editor(s). MDPI and/or the editor(s) disclaim responsibility for any injury to people or property resulting from any ideas, methods, instructions or products referred to in the content.